Journal of Magnetism and Magnetic Materials 523 (2021) 167545

Contents lists available at ScienceDirect

Journal of Magnetism and Magnetic Materials

journal homepage: www.elsevier.com/locate/jmmm

Enhanced spin Hall conductivity in tungsten-copper alloys

B. Coester [a], G.D.H. Wong [a,b], Z. Xu [a,c], J. Tang [c], W.L. Gan [a], W.S. Lew [a,*]

[a] School of Physical & Mathematical Sciences, Nanyang Technological University, 21 Nanyang Link, Singapore 637371, Singapore
[b] GLOBALFOUNDRIES Singapore Pte, Ltd., Singapore 738406, Singapore
[c] MIIT Key Laboratory of Advanced Metallic and Intermetallic Materials Technology, School of Materials Science and Engineering, Nanjing University of Science and Technology, Nanjing 210094, People's Republic of China

ARTICLE INFO

Keywords:
Thin film
Spin Hall effect
Spin Hall conductivity
Damping
Spin-torque ferromagnetic resonance

ABSTRACT

We report on the enhancement of the spin Hall conductivity in tungsten by alloying with copper, measured by using the spin-torque ferromagnetic resonance technique. The alloying leads to an increase in spin-dependent scattering events and results in an enhancement of the contributing extrinsic spin Hall effects. The measured damping property shows a slight increase with higher tungsten concentration, due to spin current losses from the ferromagnetic layer into the tungsten-copper alloy. At a tungsten concentration of 60%, the spin Hall conductivity reaches a maximum of $3.68 \pm 0.68 \times 10^5 \Omega^{-1}\mathrm{m}^{-1}$, corresponding to an enhancement of 120% compared to the pure tungsten sample. At the same concentration, the ratio of the spin Hall angle to the damping of the ferromagnetic layer, which offers a quick estimation for the critical switching current density, is found to be four times smaller as compared to pure tungsten.

1. Introduction

The realm of spintronics aims to find concepts for information transport and storage, including the spin degree of freedom of the electron. Generating spin currents efficiently is therefore of utmost importance, as it can reverse the magnetization or excite magnetization dynamics in a ferromagnet (FM). A convenient method of manipulating magnetization with spin current is through the use of the spin Hall effect (SHE) in FM/heavy metal (HM) bilayers [1–7]. While driving a charge current through the HM, the electrons gain a spin-dependent transverse velocity, thus creating a pure spin current transverse to the charge current [8,9]. This spin current can diffuse into the adjacent FM [10], exerts a spin–orbit torque (SOT) onto the magnetization, which can result in reversal [3,11,12] or oscillation [1,4].

The transverse spin-dependent velocity can have two different origins, intrinsic and extrinsic effects. While intrinsic effects are band-dependent effects [13,14], extrinsic effects are spin-dependent scattering effects like skew scattering[15] or side jump [16]. The effects become more prominent the stronger the spin–orbit coupling in the material is [17,18]. Therefore, frequently used materials are HM, like platinum (Pt) [3,14], tantalum (Ta) [4,14] and tungsten (W) [5], which have a strong spin–orbit coupling due to a high atomic number [18]. To quantify the efficiency of charge to spin current conversion and vice versa, a commonly used figure of merit is the spin Hall angle (SHA) θ_{SH} which is given by the ratio of charge current density to the spin current density [1,19].

Concerning low power consumption, it is also important to look at the spin Hall conductivity (SHC). The higher the SHC, the less energy is needed to generate the same amount of spin current [20,21]. W shows the highest SHA among 5d heavy metals in its β-phase, but it is unfavorable for device applications due to its large resistance [5,22,23]. The low resistance α-phase has a small SHA, but high SHC due to its large conductivity and is thus more favorable for applications [21]. Nevertheless, it is still important for low-power consuming devices to enhance the SHE further. It has been previously reported that the extrinsic spin Hall effects can be enhanced by means of incorporating impurities into the HM [20,24–28].

In this paper, we incorporate copper (Cu) into the highly conductive phase of tungsten (α-W) to enhance the SHE with the help of increased scattering from Cu-impurities in the alloy. At the same time Cu and α-W have low resistivities, which is supposed to maintain the SHC large, compared to highly resistive β-W. Even though β-W offers a larger SHE [5], it is metastable and tend to change into an α-W phase over time [29,30], which makes α-W more reliable for application purposes. Unfortunately, studies on SHE enhancement in α-W are still limited. Fritz et al. [31] alloyed α-W with hafnium with regards to SHE enhancement,

* Corresponding author.
E-mail address: wensiang@ntu.edu.sg (W.S. Lew).

https://doi.org/10.1016/j.jmmm.2020.167545
Received 7 August 2020; Received in revised form 23 October 2020; Accepted 2 November 2020
Available online 20 November 2020

but they did not simultaneously characterize the damping enhancement of the adjacent FM layer. However, it is very important to characterize the damping enhancement of the FM layer, because it is strongly influenced by the SHE in the adjacent layer and has a great effect on the overall power-consumption of the device stack. The damping should be kept low for more energy-efficient manipulation of the magnetization dynamics.

Therefore, spin-torque ferromagnetic resonance (ST-FMR) technique has been used to measure the SHA and damping of the system simultaneously. From the SHA and damping, the SHC has been calculated and critical switching current density behavior has been estimated. Due to a small spin–orbit coupling in Cu [32], the enhancement of the damping should remain small. Furthermore, the high heat conductivity of Cu makes it an attractive material in electronics. It has also been shown to improve spin thermoelectric devices generating spin currents via the spin Seebeck effect [33], paving the way for further applications.

The SHA and SHC are found to increase by 270% and 120%, respectively, in our set of samples at a W concentration of $x = 60\%$ compared to our sample with the pure W layer. Even though the damping of the system increases with increasing W-concentration due to the spin pumping effect, the ratio of the SHA to the damping, which allows an estimation of the critical switching current density behavior with increasing W-concentration, was found to be reduced by a factor four for this very concentration.

2. Experimental methods

Multilayer stacks of Ti(2)|Fe(5)|$Cu_{100-x}W_x$(5)|Ti(10) (nominal layer thicknesses in nanometers), with x = W-concentration in percent, were deposited by magnetron sputtering at room temperature onto thermally oxidized silicon (Si) wafers at a base pressure below 10^{-7} Torr and deposition pressure of 2 mTorr. The copper-tungsten ($Cu_{100-x}W_x$) alloy was obtained via co-sputtering where the alloy composition was controlled by varying the RF and DC power of Cu and W, respectively. RF power was used for Cu to reduce its sputtering rate while ensuring a stable plasma.

The change in composition was verified with X-ray diffraction (XRD) measurements on single layer samples of the alloy and the results are shown in Fig. 1(a). Samples with high W-concentration show W-peaks. At $x = 60\%$, the peak indicates a good crystalline α-W structure. For increasing Cu contribution, the peak shifts towards the Cu (1 1 1) peak. Additional peaks, e.g. visible for a large W content, resulting from oxidation of the single layer samples. Further, the resistivity of the samples was measured. Assuming that the current passes through all layers, the stack forms a network of parallel connected resistors and Kirchhoff's circuit law applies, using $\rho_{Ti} \approx 150 \times 10^{-8}\Omega$m for 10 nm Ti, $\rho_{Ti} \approx 360 \times 10^{-8}\Omega$m for 2 nm Ti and $\rho_{Fe} \approx 36 \times 10^{-8}\Omega$m. As shown in Fig. 1(b), the charge resistivity of the $Cu_{100-x}W_x$ alloy follows the Nordheim rule [34,35], indicating a homogenous alloy over the full range of W-concentration. The resistivity increases up to $x = 50\%$ and then decreases again, having a higher resistivity at pure W than pure Cu.

A saturation magnetization of $M_s = 1.5 \times 10^6 \mathrm{Am}^{-1}$ of the multilayer

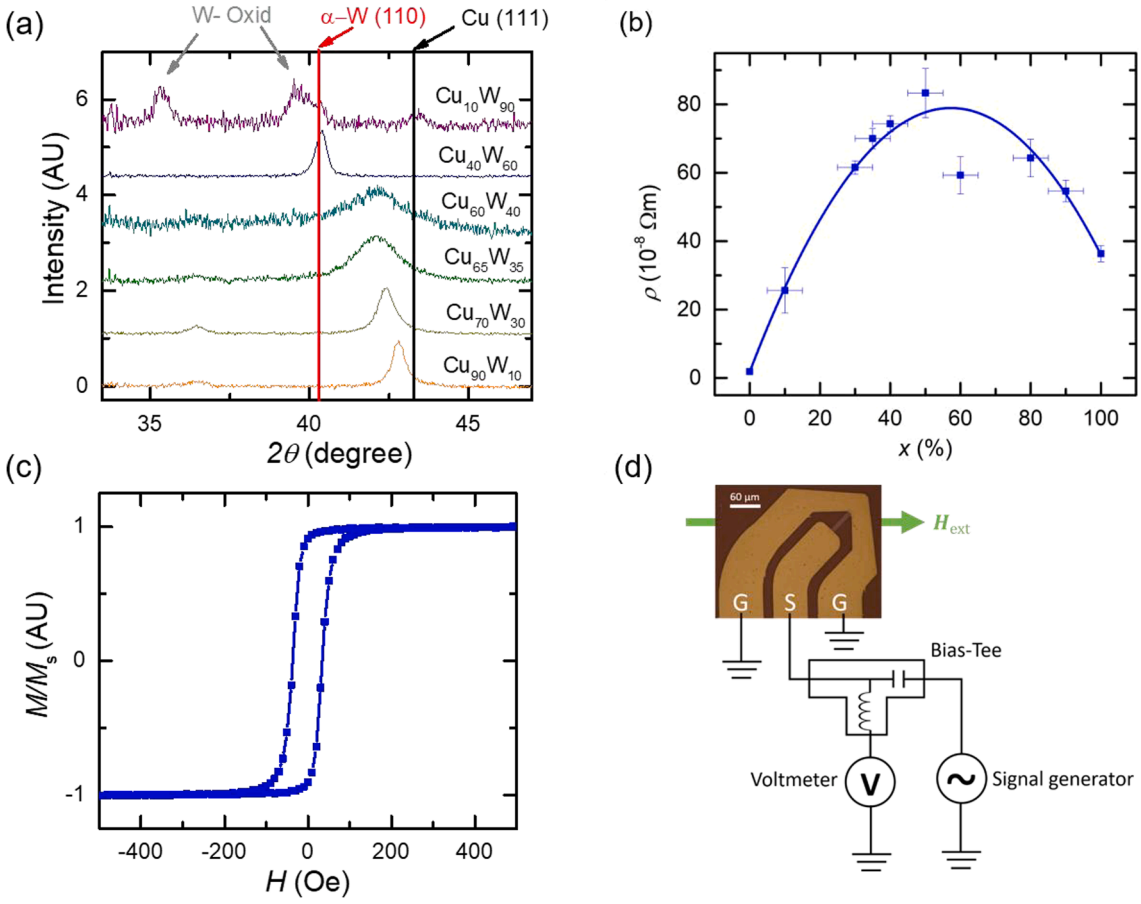

Fig. 1. (a) XRD measurements for several alloys. Samples with higher W concentration show a prominent W (1 1 0) peak, whereas for higher Cu concentration the peak shifts towards the Cu (1 1 1) peak. (b) Charge resistivity of the $Cu_{100-x}W_x$ alloy for various tungsten concentrations. (c) VSM measurements of a $Cu_{40}W_{60}$ sample with an in-plane applied magnetic field. (d) Sketch of measurement setup and microscope picture of the patterned design. The external magnetic field is applied at a 45° angle.

stacks has been measured by vibrating-sample magnetometer (VSM) measurements and an in-plane magnetization configuration was verified simultaneously. The in-plane hysteresis loop for $x = 60\%$ is presented in Fig. 1(c).

The stacks were then patterned and etched into 6 μm × 30 μm bars using electron beam lithography and ion milling techniques. In a second step, coplanar waveguides were deposited onto the samples, which connect to a ground-source-ground RF probe. The RF probe is connected to the DC + RF port of a bias-tee. The RF-port of the bias-tee is connected to a signal generator, which sends a signal at 25 dBm at a fixed frequency while an external magnetic field H_{ext} is swept from 0 Oe to 5 kOe. The alternating current I_{RF} generates a spin current due to the SHE which exerts a torque on the magnetization in the adjacent FM layer. The oscillating torque leads to continuous precession of M around the external field H_{ext} [1]. The change in the angle between magnetization and applied current results in an alternating resistance due to the anisotropic magnetoresistance (AMR) effect. The alternating current and resistance rectify to a constant voltage drop across the bar [1]. The DC voltage is picked up through the DC-port of the bias-tee with a multimeter. A sketch of the setup can be found in Fig. 1(d).

In Fig. 2(a) the measured DC voltage for several frequencies (10–15 GHz) while sweeping the magnetic field is shown. With increasing frequency, the peak broadens and shifts to higher field values as the resonance condition changes, following the Kittel equation $f_{res} = \gamma/2\pi\sqrt{H_{res}(H_{res}+4\pi M_{eff})}$ [36], where γ is the gyromagnetic ratio, H_{res} is the resonance field and $4\pi M_{eff}$ is the demagnetization field. The DC voltage can be expressed and fitted by a sum of a symmetric Lorentzian and antisymmetric Lorentzian function (Fig. 2(b)) $V_{mix} = V_0[SF_S(H_{ext}) + AF_A(H_{ext})]$, where the symmetric part arises from the SHE-induced SOT and the anti-symmetric part arises from the Oersted field induced torque [1]. V_0 is a scaling factor, $F_S(H_{ext}) = \frac{\Delta H^2}{\Delta H^2 + (H_{ext}-H_{res})^2}$ and $F_A(H_{ext}) = F_S(H_{ext})\frac{(H_{ext}-H_{res})}{\Delta H}$ where ΔH is the linewidth (half-width at half maximum) and H_{res} is the resonance field. S and A are given by $S = \left(\frac{j_s\hbar}{2e\mu_0 M_S t_{Fe}}\right)$ and $A = \left(\frac{j_c t_{CuW}}{2}\right)\left[\frac{4\pi M_{eff}}{H_{ext}}\right]^{1/2}$, thus SHA can be obtained from the parameters S and A via [1]

$$\theta_{SH} = \frac{j_s}{j_c} = \left(\frac{S}{A}\right)\left(\frac{e\mu_0 M_S t_{Fe} t_{CuW}}{\hbar}\right)\left[1 + \frac{4\pi M_{eff}}{H_{ext}}\right]^{1/2} \quad (1)$$

where j_s is the spin current density, j_c is the charge current density, $\hbar$ is the reduced Planck constant, e is the electron charge, M_S is the saturation magnetization, t_{Fe} is the thickness of the Fe layer and t_{CuW} is the alloy layer thickness.

Another important parameter is the effective damping of the ferromagnetic layer, which can be extracted from the linewidth ΔH. In Fig. 2 (d), the linewidth was observed to follow a linear function when plotted

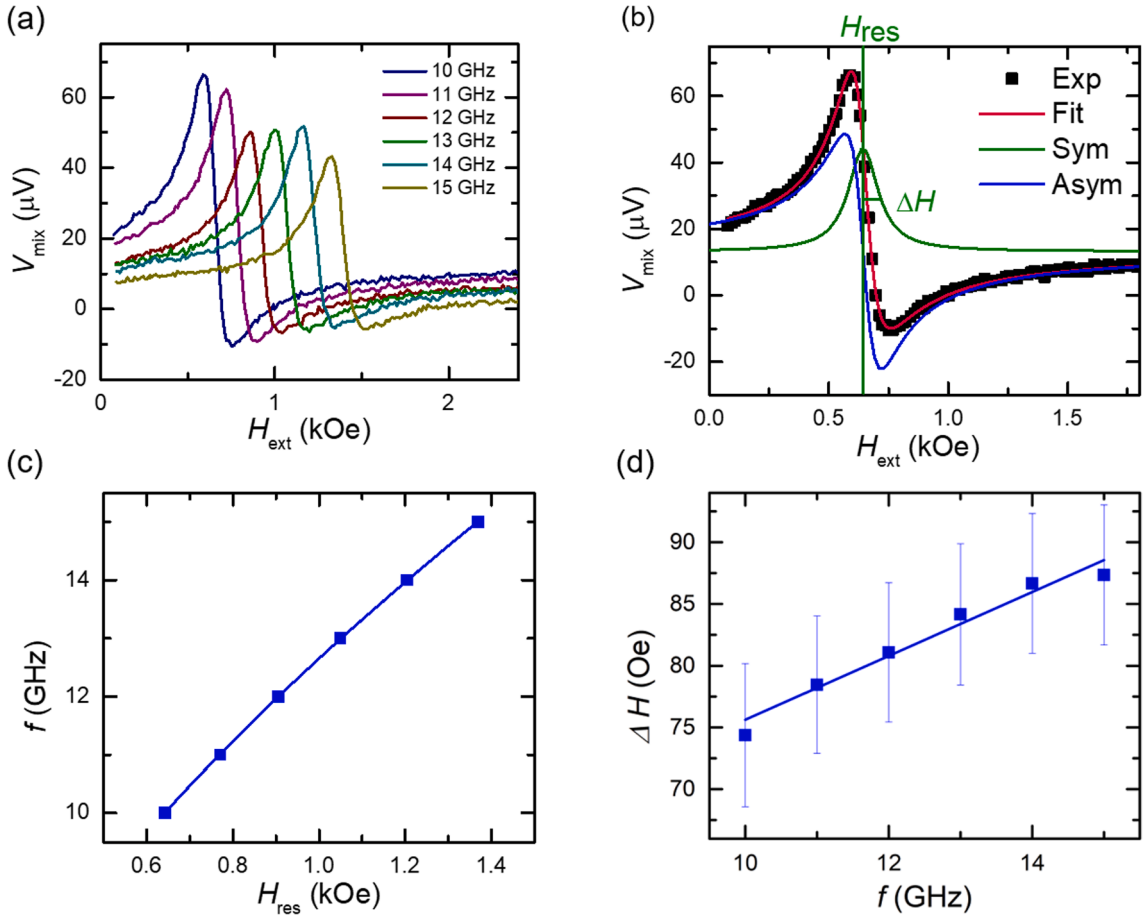

Fig 2. (a) Measured V_{mix} signals at different frequencies. Peaks shifting from left to right with higher frequency. (b) Black squares show the measurement data for 10 GHz, red is the corresponding fit. The green and blue lines are the symmetric and antisymmetric Lorentzian functions, respectively. (c) The resonance frequencies are plotted against the extracted resonance fields and fitted with the Kittel equation [36]. (d) Linewidth (half-width at half maximum) over frequency plot. The slope of the linear fit is proportional to the damping factor. All data origin from the $Cu_{40}W_{60}$ sample. The Landé g factor and gyromagnetic ratio γ are determined from the Kittel equation and are on average for all samples 2.16 ± 0.05 and $30,355 \pm 674$ MHz/T, respectively. (For interpretation of the references to colour in this figure legend, the reader is referred to the web version of this article.)

over the frequency and its slope is proportional to the effective damping α_{eff} [37,38]:

$$\Delta H = \Delta H_0 + \frac{2\pi\alpha_{\mathrm{eff}}}{\gamma} f \tag{2}$$

where ΔH_0 is the linewidth offset induced by magnetic inhomogeneities [39]. The gyromagnetic ratio γ is taken from the Kittel fitting for the resonance conditions in Fig. 2(c).

3. Results and discussion

The SHA for the different W-concentration x is plotted in Fig. 3(a). In the Cu-rich regime ($x < 35\%$), the SHA is very small as to be expected for Cu [32]. For $x = 35\%$, the SHA is the same as for pure W, *i.e.* to convert the same amount of spin current into charge current as a pure W layer, only an addition of 35% W into Cu is needed. When more W is added, the SHA increases further and reaches a maximum of $\theta_{SH} = 0.20 \pm 0.02$ at $x = 60\%$. For higher W concentrations, the SHA reduces monotonically to the value of pure W. With $\theta_{SH} = 0.054 \pm 0.004$ for pure W, it is close to the measured upper bound of the SHA found for α-W in Ref [5]. As compared to the here measured pure W sample, the SHA of $Cu_{40}W_{60}$ is enhanced by about 270%. The maximum value of 0.20 ± 0.02 is close to values determined for an α-β mixed phase of W [5] or to an alloy of rare-earth and α-W measured by Fritz et al. [31]. This shows that by simply adding Cu to W similarly high SHA can be achieved. Even though β-W has a larger SHA, it is metastable and is known to transform into an α-phase over time [29,30].

Dividing the SHA by the charge resistivity, leads to the SHC [20],

$$\sigma_{\mathrm{SH}} = \frac{\hbar}{2e}\theta_{\mathrm{SH}}\frac{1}{\rho_{\mathrm{CuW}}} \tag{3}$$

It is shown in Fig. 3(b), except for the pure Cu sample, which does not give a realistic SHC due to its low SHA and resistivity. At a concentration of $x = 60\%$ the alloy has the highest SHC. A very large SHA and comparably low resistivity lead to a large SHC in comparison with the rest of the alloys. This means at $x = 60\%$ a large spin current can be generated with less dissipation, i.e. more energy efficient.

By using the ST-FMR technique, it is possible to extract information about the effective damping of the FM layer concurrently. Fig. 4(a) shows the effective damping of the Fe layer, which increases from pure Cu to pure W. This increase in the effective damping results from spin pumping, which is the transfer of spin current from the FM layer, originating from magnetization dynamics, into the adjacent heavy metal layer [40–46]. This lost spin current leads to a faster relaxation of the oscillating magnetization and is thus measurable as enhanced damping [42]. Typically, materials with large SHA also show large spin pumping effects [42–46], and thus it is not surprising that both W-phases show higher spin pumping enhancement than Cu [45].

However, not only spin pumping but also interface effects can affect the damping as well as the SHA [47–51]. At the interface, the spin is not conserved, therefore additional spin flip occurs and leads to spin memory loss [48–50]. Furthermore, the current crossing the interface depends on the effective spin mixing conductance, which represents the efficiency of the spin angular momentum transferred across the HM/FM interface [10,52–56]. The effective spin mixing conductance depends on the spin current backflow, i.e. spin current flowing back into the FM, which decreases the damping enhancement [57]. Since spin memory loss and spin current backflow are determined by interface conditions [58], they play a major role. The fluctuations in the presented damping parameter in Fig. 4(a), could result from differences in the interface condition, such as intermixing. An estimation of the efficiency, with that the spin current is transferred across the interface, can be made by calculating the effective spin mixing conductance $g^{\uparrow\downarrow}{}_{eff}$ [32,59]:

$$g^{\uparrow\downarrow}{}_{eff} = \frac{4\pi M_s t_{\mathrm{FM}}}{g\mu_{\mathrm{B}}}\left(\alpha_{\mathrm{eff,CuW|Fe}} - \alpha_{\mathrm{eff,Cu|Fe}}\right) \tag{4}$$

Here, the sample with the pure Cu layer on Fe is used as reference sample, because Cu has only small spin–orbit coupling and spin pumping effect, respectively [32]. It must be noted, that it thus only represents an upper bound for the effective spin mixing conductance, which reaches a maximum value of $24.5 \pm 5.9\mathrm{nm}^{-2}$ for the pure W sample. Results are presented in the inset of Fig. 4(a) together with the effective damping parameter.

However, further consideration of the interface quality exceeds the scope of this work. It is therefore appropriate to regard the here measured SHA as an effective SHA, since we do not differentiate between bulk contributions of the HM and HM|FM interface contributions, but the overall effectively measured charge to spin current conversion efficiency.

For a practical spintronics device, the critical magnetization switching current density is of utmost importance. It is given by [6,60]

$$j_{\mathrm{crit}} \approx \frac{2e}{\hbar}\left(\frac{\alpha_{\mathrm{eff}}}{\theta_{\mathrm{SH}}}\right)\left(\frac{4\pi M_{eff}}{2}\right) M_S t_{\mathrm{Fe}} \tag{5}$$

The trend of the critical switching current density is mainly determined by the ratio of $\frac{\alpha_{\mathrm{eff}}}{\theta_{\mathrm{SH}}}$, as plotted in Fig. 4(b). Due to the very small SHA for the Cu-rich alloys, the critical switching current density becomes very large. For this reason, only the concentration-dependent

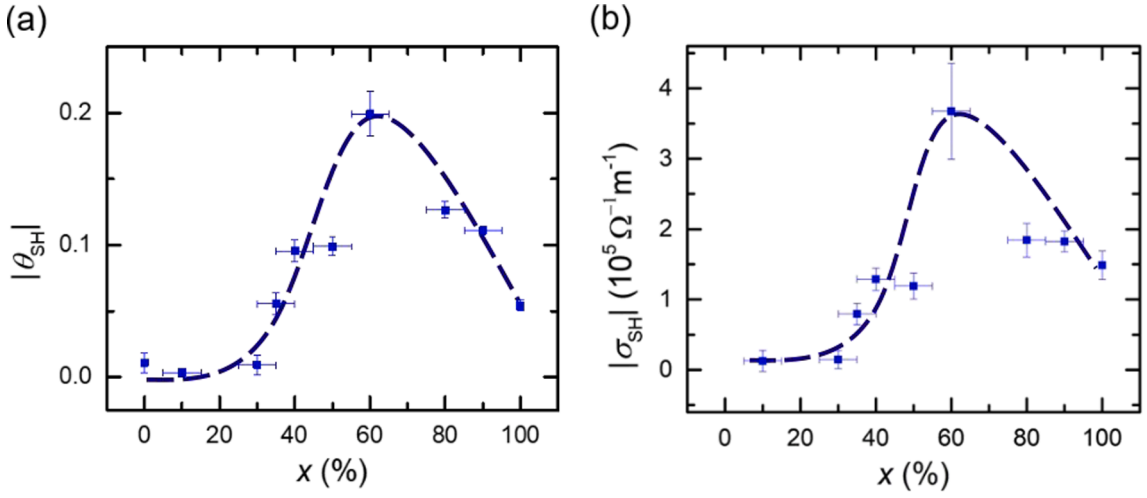

Fig 3. (a) SHA θ_{SH} and (b) SHC σ_{SH} for various W-concentration in the $Cu_{100-x}W_x$ alloy. Note that the pure Cu sample ($x = 0\%$) does not give a realistic SHC due to its low SHA and resistivity and is thus omitted from this plot. The dashed lines serve as a guide-to-the-eye.

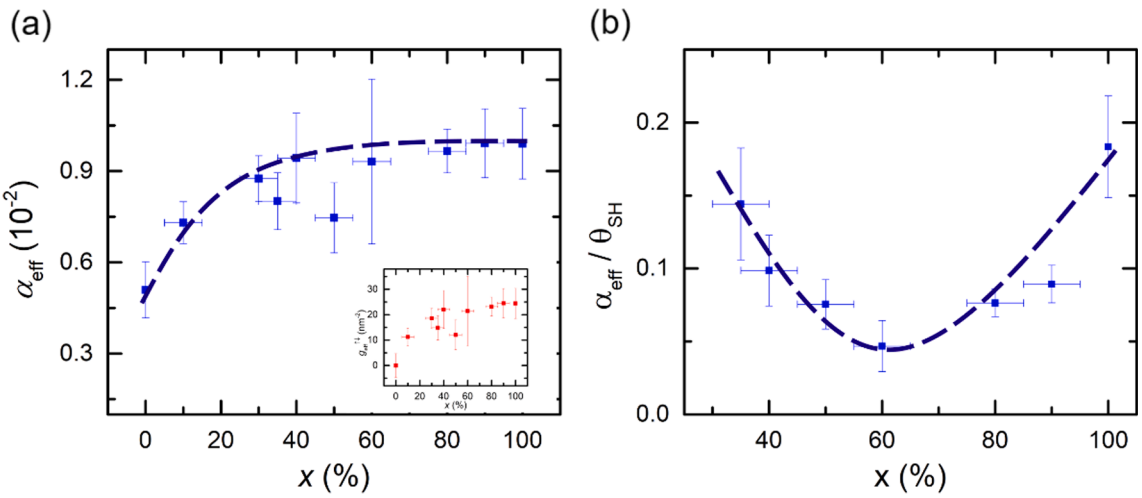

Fig 4. For various tungsten concentration in the $Cu_{100-x}W_x$ alloy (a) damping factor and effective spin mixing conductance (inset), (b) ratio of damping and SHA, determining the critical switching current density for an in-plane magnetized material. Due to a very small SHA the lower concentrations have been omitted from this plot. The dashed lines serve as a guide-to-the-eye.

behavior for $x = 35\%$ onwards are presented. Since the SHA is the highest at $x = 60\%$, the critical switching current density has the lowest value at that concentration. At this optimal combination, the ratio of the SHA and damping undergoes a reduction of a factor of four as compared to the pure W sample. Considering that the trend of $\frac{\alpha_{eff}}{\theta_{SH}}$ being almost the reverse of SHA, changes in the effective damping do not have a large impact. The order of magnitude stays the same for the damping, whereas the changes in SHA are more prominent.

To understand more about the importance of this ratio, we compare our $\frac{\alpha_{eff}}{\theta_{SH}}$ to Ref. [32], where different metals on yttrium iron garnet were investigated, and to Ref [61], where gold (Au) was alloyed with W at a W-concentration of 7% on permalloy (Py) ($Au_{93}W_7$|Py). The values for the effective damping α_{eff}, the SHA θ_{SH}, their ratio $\frac{\alpha_{eff}}{\theta_{SH}}$, the resistivity ρ and the ratio of SHA and ρ, *i.e.* SHC σ_{SH} are presented in Table 1. For each parameter, the most optimal one is presented in bold text, while the least optimal is presented in italic.

For β-W on YIG, the comparably high SHA and low damping favor a very low $\frac{\alpha_{eff}}{\theta_{SH}}$. Despite the $Cu_{40}W_{60}$|Fe sample has the largest effective damping among the presented stacks it can be easily compensated with an enhanced SHA, which leads to the high SHC of $3.68 \pm 0.68 \times 10^5 \Omega^{-1}m^{-1}$. Noting that for $Au_{93}W_7$|Py the SHA might increase with a thinner $Au_{93}W_7$ layer in Ref. [61], the charge resistivity would increase at the same time. Therefore, even if reaching a better critical switching current density, the SHC would decrease, *i.e.* pure spin current generation would be less energy efficient.

These comparisons emphasize the importance of a tradeoff of material parameters. A higher resistivity usually benefits a large SHA, which at the same time decreases j_{crit}. But for a more energy-efficient spin current generation one has also to keep the SHC in mind, which benefits from a lower resistivity.

4. Conclusion

In conclusion, we have investigated the SOT efficiency of copper-tungsten alloys over a wide range of concentrations by means of ST-FMR. A SHA of 0.20 ± 0.02 was measured for a concentration combination of $Cu_{40}W_{60}$. This corresponds to an enhancement of 270% as compared to pure W. With the simultaneously extracted information about the damping of the FM layer, it was found that the ratio of damping and SHA, which is proportional to the critical switching current density for in-plane magnetization, can be reduced by a factor four at a W-concentration of $x = 60\%$ compared to pure W. This makes $Cu_{40}W_{60}$|Fe a promising candidate for energy efficient applications, such as spin Hall nano-oscillator or spin–orbit torque-driven memory devices.

Table 1
Effective damping α_{eff}, SHA θ_{SH}, their ratio $\frac{\alpha_{eff}}{\theta_{SH}}$, the resistivity ρ and SHC σ_{SH} are presented for different HM|FM stacks. For each parameter, the most optimal one is presented in bold, while the least optimal is presented in italic.

Material stack	$\alpha_{eff}(10^{-2})$	θ_{SH}	$\frac{\alpha_{eff}}{\theta_{SH}}$	$\rho(10^{-8}\Omega m)$	$\sigma_{SH}(10^5\Omega^{-1}m^{-1})$
Cu|YIG [32]	**0.2**	*0.003*	*0.54*	**6.3**	*0.51*
β-W|YIG [32]	0.3	0.14	**0.02**	*180*	0.78
$Au_{93}W_7$|Py [61]	0.8	0.10	0.08	57.0	1.75
$Cu_{40}W_{60}$|Fe (this work)	*0.9*	**0.20**	0.05	54.2	**3.68**

CRediT authorship contribution statement

B. Coester: Conceptualization, Investigation, Validation, Formal analysis, Writing - original draft. **G.D.H. Wong:** Conceptualization, Software, Writing - review & editing. **Z. Xu:** Conceptualization, Writing - review & editing. **J. Tang:** Investigation, Writing - review & editing. **W. L. Gan:** Writing - review & editing. **W.S. Lew:** Supervision, Funding acquisition.

Declaration of Competing Interest

The authors declare that they do not have any known competing financial interests or personal relationships that could have appeared to influence the work reported in this paper.

Acknowledgements

The work was supported by the Singapore National Research Foundation, under a Competitive Research Programme (Non-volatile Magnetic Logic and Memory Integrated Circuit Devices, NRF-CRP9-2011-01), and an Industry-IHL Partnership Program (NRF2015- IIP001-001). The support from an RIE2020 ASTAR AME IAF-ICP Grant (No. I1801E0030) is also acknowledged.

Appendix A. Supplementary data

Supplementary data to this article can be found online at https://doi.

org/10.1016/j.jmmm.2020.167545.

References

[1] L. Liu, et al., Spin-torque ferromagnetic resonance induced by the spin Hall effect, Phys. Rev. Lett. 106 (3) (2011), 036601.
[2] J. Kim, et al., Spin Hall Magnetoresistance in Metallic Bilayers, Phys. Rev. Lett. 116 (9) (2016), 097201.
[3] L. Liu, et al., Current-induced switching of perpendicularly magnetized magnetic layers using spin torque from the spin Hall effect, Phys. Rev. Lett. 109 (9) (2012), 096602.
[4] L. Liu, et al., Spin-torque switching with the giant spin hall effect of tantalum, Science 336 (6081) (2012) 555.
[5] C.-F. Pai, et al., Spin transfer torque devices utilizing the giant spin Hall effect of tungsten, Appl. Phys. Lett. 101 (12) (2012), 122404.
[6] K.-S. Lee, et al., Threshold current for switching of a perpendicular magnetic layer induced by spin Hall effect, Appl. Phys. Lett. 102 (11) (2013), 112410.
[7] F. Luo, et al., Dependence of spin-orbit torque effective fields on magnetization uniformity in Ta/Co/Pt structure, Sci. Rep. 9 (1) (2019) 10776.
[8] M. Althammer, Pure spin currents in magnetically ordered insulator/normal metal heterostructures, J. Phys. D Appl. Phys. 51 (31) (2018), 313001.
[9] F. Freimuth, S. Blügel, Y. Mokrousov, Anisotropic Spin hall effect from first principles, Phys. Rev. Lett. 105 (24) (2010), 246602.
[10] A. Brataas, Y.V. Nazarov, G.E.W. Bauer, Finite-element theory of transport in ferromagnet-normal metal systems, Phys. Rev. Lett. 84 (11) (2000) 2481–2484.
[11] I.M. Miron, et al., Perpendicular switching of a single ferromagnetic layer induced by in-plane current injection, Nature 476 (7359) (2011) 189–193.
[12] S. Li, et al., Deterministic spin-orbit torque induced magnetization reversal in Pt/[Co/Ni]n/Co/Ta multilayer hall bars, Sci. Rep. 7 (1) (2017) 972.
[13] D. Xiao, M.-C. Chang, Q. Niu, Berry phase effects on electronic properties, Rev. Mod. Phys. 82 (3) (2010) 1959–2007.
[14] M. Morota, et al., Indication of intrinsic spin Hall effect in 4d and 5d transition metals, Phys. Rev. B 83 (17) (2011), 174405.
[15] J. Smit, The spontaneous hall effect in ferromagnetics II, Physica 24 (1) (1958) 39–51.
[16] L. Berger, Side-jump mechanism for the hall effect of ferromagnets, Phys. Rev. B 2 (11) (1970) 4559–4566.
[17] M.I. Dyakonov, V.I. Perel, Current-induced spin orientation of electrons in semiconductors, Phys. Lett. A 35 (6) (1971) 459–460.
[18] M.I. Dyakonov (Ed.), Spin physics in semiconductors, second ed. Springer series in solid-state sciences, volume 157, Cham, Switzerland: Springer, 2017.
[19] M. Isasa, et al., Temperature dependence of spin diffusion length and spin Hall angle in Au and Pt, Phys. Rev. B 91 (2) (2015), 024402.
[20] M. Obstbaum, et al., Tuning spin hall angles by alloying, Phys. Rev. Lett. 117 (16) (2016), 167204.
[21] W.-B. Liao, et al., Current-Induced Magnetization Switching by the High Spin Hall Conductivity α-W, Phys. Status Solidi (RRL) – Rapid Res. Lett. 13 (11) (2019) 1900408.
[22] H.L. Wang, et al., Large spin pumping from epitaxial $Y_3Fe_5O_{12}$ thin films to Pt and W layers, Phys. Rev. B 88 (10) (2013), 100406.
[23] J. Liu, et al., Correlation between the spin Hall angle and the structural phases of early 5d transition metals, Appl. Phys. Lett. 107 (23) (2015), 232408.
[24] L. Zhu, D.C. Ralph, R.A. Buhrman, Highly efficient spin-current generation by the spin Hall effect in $Au_{1-x}Pt_x$, Phys. Rev. Appl. 10 (3) (2018), 031001.
[25] R. Ramaswamy, et al., Extrinsic Spin hall effect in $Cu_{1-x}Pt_x$, Phys. Rev. Appl. 8 (2) (2017), 024034.
[26] A. Musha, Y. Kanno, K. Ando, Extrinsic-intrinsic crossover of the spin Hall effect induced by alloying, Phys. Rev. Mater. 3 (5) (2019), 054411.
[27] G.D.H. Wong, et al., Thermal behavior of spin-current generation in PtxCu1-x devices characterized through spin-torque ferromagnetic resonance, Sci. Rep. 10 (1) (2020) 9631.
[28] Z. Xu, et al., Giant spin Hall effect in Cu–Tb alloy thin films, ACS Appl. Mater. Interfaces (2020).
[29] S.M. Rossnagel, I.C. Noyan, C.C. Jr, Phase transformation of thin sputter-deposited tungsten films at room temperature, J. Vacuum Sci. Technol. B: Microelectron. Nanometer Struct. Process. Meas. Phenomena 20 (5) (2002) 2047–2051.
[30] J. Xiao, et al., Super-stable ultrafine beta-tungsten nanocrystals with metastable phase and related magnetism, Nanoscale 5 (3) (2013) 899–903.
[31] K. Fritz, et al., Large spin Hall effect in an amorphous binary alloy, Phys. Rev. B 98 (9) (2018), 094433.
[32] H.L. Wang, et al., Scaling of spin Hall Angle in 3d, 4d, and 5d metals from $Y_3Fe_5O_{12}$/metal spin pumping, Phys. Rev. Lett. 112 (19) (2014), 197201.
[33] K. Tian, A. Tiwari, CuPt alloy thin films for application in spin thermoelectrics, Sci. Rep. 9 (1) (2019) 3133.
[34] L. Nordheim, Zur Elektronentheorie der Metalle, II. Ann. Phys. 401 (6) (1931) 641–678.
[35] K.L. Chopra, et al., Electron transport properties of amorphous Cu-Ag films, Phys. Status Solidi (a) 40(1) (1977) 247–255.
[36] C. Kittel, On the Theory of Ferromagnetic Resonance Absorption, Phys. Rev. 73 (2) (1948) 155–161.
[37] H.T. Nembach, et al., Perpendicular ferromagnetic resonance measurements of damping and Lande g-factor in sputtered $(Co_2Mn)_{1-x}Ge_x$ thin films, Phys. Rev. B 84 (5) (2011), 054424.
[38] J.M. Shaw, H.T. Nembach, T.J. Silva, Determination of spin pumping as a source of linewidth in sputtered $Co_{90}Fe_{10}$/Pd multilayers by use of broadband ferromagnetic resonance spectroscopy, Phys. Rev. B 85 (5) (2012), 054412.
[39] M. Weiler, et al., Spin pumping and spin currents in magnetic insulators, in: Solid State Physics, Elsevier, 2013, pp. 123–156.
[40] M.A.W. Schoen, et al., Ultra-low magnetic damping of a metallic ferromagnet, Nat. Phys. 12 (9) (2016) 839–842.
[41] M.A.W. Schoen, et al., Magnetic properties in ultrathin $3d$ transition-metal binary alloys. II. Experimental verification of quantitative theories of damping and spin pumping, Phys. Rev. B 95 (13) (2017), 134411.
[42] Y. Tserkovnyak, A. Brataas, G.E.W. Bauer, Enhanced gilbert damping in thin ferromagnetic films, Phys. Rev. Lett. 88 (11) (2002), 117601.
[43] M. Haertinger, et al., Spin pumping in YIG/Pt bilayers as a function of layer thickness, Phys. Rev. B 92 (5) (2015), 054437.
[44] S. Mizukami, Y. Ando, T. Miyazaki, Ferromagnetic resonance linewidth for NM/80NiFe/NM films (NM=Cu, Ta, Pd and Pt), J. Magn. Magn. Mater. 226–230 (2001) 1640–1642.
[45] D. Jhajhria, et al., Dependence of spin pumping in W/CoFeB heterostructures on the structural phase of tungsten, Phys. Rev. B 99 (1) (2019), 014430.
[46] S. Kasai, et al., Modulation of effective damping constant using spin Hall effect, Appl. Phys. Lett. 104 (9) (2014), 092408.
[47] L. Zhu, D.C. Ralph, R.A. Buhrman, Effective spin-mixing conductance of heavy-metal–ferromagnet interfaces, Phys. Rev. Lett. 123 (5) (2019), 057203.
[48] J.C. Rojas-Sánchez, et al., Spin pumping and inverse spin Hall effect in platinum: the essential role of spin-memory loss at metallic interfaces, Phys. Rev. Lett. 112 (10) (2014), 106602.
[49] Y. Liu, et al., Interface enhancement of gilbert damping from first principles, Phys. Rev. Lett. 113 (20) (2014), 207202.
[50] K. Gupta, et al., Disorder dependence of interface spin memory loss, Phys. Rev. Lett. 124 (8) (2020), 087702.
[51] L. Wang, et al., Giant room temperature interface spin hall and inverse spin Hall effects, Phys. Rev. Lett. 116 (19) (2016), 196602.
[52] K. Xia, et al., Spin torques in ferromagnetic/normal-metal structures, Phys. Rev. B 65 (22) (2002), 220401.
[53] X. Waintal, et al., Role of spin-dependent interface scattering in generating current-induced torques in magnetic multilayers, Phys. Rev. B 62 (18) (2000) 12317–12327.
[54] Y. Tserkovnyak, A. Brataas, G.E.W. Bauer, Spin pumping and magnetization dynamics in metallic multilayers, Phys. Rev. B 66 (22) (2002), 224403.
[55] A. Brataas, Y.V. Nazarov, G.E.W. Bauer, Spin-transport in multi-terminal normal metal-ferromagnet systems with non-collinear magnetizations, Eur. Phys. J. B – Condens. Matter Complex Syst. 22 (1) (2001) 99–110.
[56] S.A. Bender, Y. Tserkovnyak, Interfacial spin and heat transfer between metals and magnetic insulators, Phys. Rev. B 91 (14) (2015), 140402.
[57] M. Weiler, et al., Experimental test of the spin mixing interface conductivity concept, Phys. Rev. Lett. 111 (17) (2013), 176601.
[58] L. Zhu, D.C. Ralph, R.A. Buhrman, Enhancement of spin transparency by interfacial alloying, Phys. Rev. B 99 (18) (2019), 180404.
[59] O. Mosendz, et al., Detection and quantification of inverse spin Hall effect from spin pumping in permalloy/normal metal bilayers, Phys. Rev. B 82 (21) (2010), 214403.
[60] L. Huang, et al., Engineering magnetic heterostructures to obtain large spin Hall efficiency for spin-orbit torque devices, Appl. Phys. Lett. 113 (2) (2018), 022402.
[61] P. Laczkowski, et al., Experimental evidences of a large extrinsic spin Hall effect in AuW alloy, Appl. Phys. Lett. 104 (14) (2014), 142403.